JTAE

E- ISSN: 2676-4253

Journal of Technology in Aerospace Engineering

Vol. VV, No. NN, pp. 1-10, YYYY

https://doi.org/10.22034/jtae.yyyy.nnnn

Journal Homepage: https://www.jtae.ari.ac.ir

Technical Note

Numerical Study of Plasma Actuator Placement for Flow Separation Control on a NACA 6412 Airfoil

Arash Divazi[1], Erfan Noferesti[2], and Majid Hajipourm[3*]

College of Interdisciplinary Science and Technology, University of Tehran, Tehran, Iran
Department of Mechanical Engineering, University of Naples Federico ii, Naples, Italy
College of Interdisciplinary Science and Technology, University of Tehran, Tehran, Iran

ARTICLE INFO

Article History:

Received 26 August 2025
Revised 30 August 2025
Acceptet 28 October 2025
Available Online 08 December 2025

Keywords:

Flow control
DBD plasma actuator
Separation control
Momentum injection
NACA 6412

ABSTRACT

We numerically assess how chordwise placement of a single dielectric barrier discharge (DBD) plasma actuator affects separation control on a cambered NACA 6412 airfoil at $\alpha = 12°$ for $U_\infty = 1$ and 10 m/s ($Re \approx 6.85\times10^4$ and 6.85×10^5, respectively). Steady RANS (SST k-ω) is coupled with a Shyy-type body-force model to represent the actuator. In the baseline, separation forms on the suction side with onset near $x/c \approx 0.60$ at 1 m/s and $x/c \approx 0.70$ at 10 m/s. Four plasma actuator locations are evaluated: $x/c = 0.03$ (LEL), 0.10 (LER), 0.40 (TEL), and 0.65 (TER). Simulation results indicated that placement strongly governs authority by determining where momentum is added to the boundary layer. A leading-edge actuator at $x/c \approx 0.03$ consistently yields the best outcome, delaying or removing separation, strengthening the suction peak, and promoting smooth pressure recovery, especially at 10 m/s. A downstream actuator near $x/c \approx 0.65$ is the next most effective, targeting the vicinity of natural separation. LER ($x/c \approx 0.10$) is the least effective, especially at 10 m/s, where residual trailing-edge separation remains. For placements aft of the maximum thickness, very strong actuation (plasma jet ≫ free-stream) can induce a laminar separation bubble and increase drag despite lift gains. These findings offer practical guidance for selecting actuator position and strength on cambered airfoils at moderate incidence.

* Corresponding Author's E-mail: hajipourm@ut.ac.ir

How to Cite this Article:
A. Divazi, E. Noferesti, and M. Hajipourm, "Numerical study of plasma actuator placement for flow separation control on a NACA 6412 airfoil," *Journal of technology in aerospace engineering*, Vol. VV, Special Issue, pp. 1-10, YYYY, https://doi.org/10.22034/jtae.yyyy.nnnn.

1 INTRODUCTION

Active flow control (AFC) techniques have garnered significant interest in modern aerodynamics for their potential to reduce drag, enhance lift, and improve overall aerodynamic efficiency [1]. Among these, dielectric barrier discharge (DBD) plasma actuators are particularly promising due to their rapid response, absence of moving parts, and ease of integration with aerodynamic surfaces [2].

DBD actuators function by generating a low-temperature plasma between asymmetric electrodes when subjected to a high-voltage alternating current [3]. The surrounding air is ionized, and the resulting charged particles are accelerated by the electric field, producing a body force known as electrohydrodynamic (EHD) force. This force transfers momentum to the near-wall fluid, generating an induced flow (often described as a pseudo wall jet) that can suppress or delay boundary layer separation [4]. The modification of the near-wall flow structure plays a critical role in delaying or mitigating flow separation [5].

A key determinant of DBD actuator performance is its placement on the airfoil surface [6]. Actuator location influences boundary layer behavior, vortex shedding, and stall onset, all of which affect aerodynamic performance. Actuators placed near the leading edge are typically effective in delaying separation, whereas those positioned toward the trailing edge may enhance circulation and manage wake structures [7]. Optimal placement depends on several aerodynamic parameters, such as Reynolds number, angle of attack, and airfoil geometry [3].

Ogawa et al. [8] used large-eddy simulations to evaluate DBD plasma actuator performance on an airfoil at pre-stall angles of attack. Their results showed that, near stall, DBD actuation promotes early turbulent transition and facilitates flow reattachment. At lower angles, vortex-induced momentum transport helps maintain attached flow. Wang et al. [9] performed low-speed wind tunnel experiments to study plasma flow control effects on airfoil performance. They observed improvements in both maximum lift and stall angle for symmetric and high-lift airfoils. Khoshkoo et al. [10] employed numerical simulations to investigate the effect of steady plasma body forces on stalled NACA 0015 flow fields. Their findings confirm the effectiveness of DBD actuators in mitigating separation at low Reynolds numbers.

Kelley et al. [11] conducted compressible wind tunnel tests using AC DBD actuators to suppress leading-edge stall on a NASA energy-efficient transport airfoil. They reported effective reattachment of separated flow, leading to increased maximum lift and delayed stall. Little et al. [12] studied separation control on a deflected high-lift airfoil flap at Reynolds numbers up to 240,000 using a single DBD actuator placed near the flap shoulder. They concluded that the actuator enhanced natural vortex shedding, which improved momentum exchange between the freestream and separated region.

While previous studies have demonstrated the general effectiveness of DBD plasma actuators for flow separation control, the influence of actuator placement on specific airfoil geometries, particularly under moderate angles of attack, remains insufficiently characterized. Moreover, most existing numerical investigations have focused on symmetric or generic airfoils, leaving a gap in understanding for cambered airfoils like the NACA 6412, which are commonly used in practical applications. Additionally, the spatial sensitivity of actuator-induced flow control, especially in streamwise configurations, warrants further exploration using high-resolution simulation techniques.

In this work, we investigate how chordwise placement of a DBD actuator affects the aerodynamics of a cambered NACA 6412 airfoil at $\alpha = 12°$, using computational fluid dynamics (CFD). Four locations are examined, at $x/c = 0.03$, 0.10, 0.40, and 0.65. The actuator is represented with a Shyy-type body-force model within steady Reynolds-averaged Navier–Stokes simulations using the SST k–ω turbulence model. For a 1 m chord and $U_\infty = 1$ and 10 m/s, the corresponding Reynolds numbers are $Re \approx 6.8 \times 10^4$ and $Re \approx 6.8 \times 10^5$. The objective is to map the placement dependence of separation control and provide practical guidance for selecting actuator location and strength to enhance lift and mitigate separation in low-to-moderate Reynolds-number regimes.

2 MATERIAL and METHODS

Flow separation is a fundamental aerodynamic phenomenon that occurs when the boundary layer is unable to overcome an adverse pressure gradient (APG), leading to a reversal of flow near the surface. Mathematically, this is characterized by the streamwise velocity gradient normal to the wall, $\partial u/\partial y$, approaching zero and subsequently becoming negative [13]. The magnitude of this gradient reflects the "fullness" of the velocity profile: a more positive value corresponds to higher near-wall momentum and a more stable boundary layer.

As illustrated in Figure 1, the shape of the velocity profile, and by extension, the likelihood of flow separation, is influenced by multiple factors. These include external momentum sources (e.g., flow injection), momentum sinks (e.g., suction), and the viscous dissipation inherent in the flow. Viscous effects always act to dissipate momentum, and their influence is especially critical in the near-wall region where frictional forces dominate.

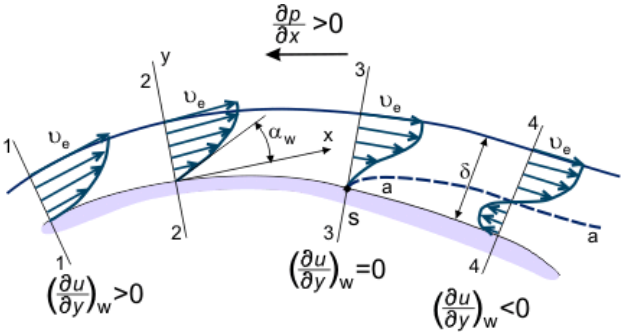

Fig. 1. Flow separation due to adverse pressure gradient, illustrating velocity profile reversal near the wall [14].

Among these influences, the adverse pressure gradient plays a central role: as pressure increases in the direction of flow, the kinetic energy of the boundary layer decreases, weakening its ability to remain attached. Understanding the interaction between APG and flow momentum is essential for designing effective flow control strategies, such as those involving plasma actuators. In this context, a quantitative understanding of separation behavior is critical for validating and evaluating the effectiveness of body-force-based actuation models in CFD simulations.

2.1 Governing Equations

The computational model used in this study is based on the two-dimensional, steady-state, incompressible Reynolds-Averaged Navier–Stokes (RANS) equations, supplemented with a body force term to represent the effect of the plasma actuator [15], [16].

The conservation of mass is enforced via the continuity equation:

$$\frac{\partial u}{\partial x} + \frac{\partial v}{\partial y} = 0 \tag{1}$$

where u and v are the velocity components in the streamwise (x) and wall-normal (y) directions, respectively.

The momentum equations in the x- and y-directions include contributions from pressure, viscous diffusion, and external forcing. The x-momentum equation incorporates the plasma actuator body force f_x:

$$u\frac{\partial u}{\partial x} + v\frac{\partial u}{\partial y} = -\left(\frac{1}{\rho}\right)\frac{\partial p}{\partial x} + \nu\left(\frac{\partial^2 u}{\partial x^2} + \frac{\partial^2 u}{\partial y^2}\right) + f_x \tag{2}$$

where p is the static pressure, ρ is the fluid density (assumed constant for incompressible flow), ν=μ/ρ is the kinematic viscosity, μ is the dynamic viscosity, and f_x represents the plasma actuator body force in the streamwise (x) direction.

The y-momentum equation incorporates the plasma actuator body force f_y:

$$u\frac{\partial v}{\partial x} + v\frac{\partial v}{\partial y} = -\left(\frac{1}{\rho}\right)\frac{\partial p}{\partial y} + \nu\left(\frac{\partial^2 v}{\partial x^2} + \frac{\partial^2 v}{\partial y^2}\right) + f_y \tag{3}$$

The turbulence closure is achieved using the k–ω SST model, which is well-suited for resolving adverse pressure gradients and flow separation, conditions critical for accurate simulation of plasma-induced control. The turbulent kinetic energy k is governed by:

$$\nabla \cdot (\rho u k) = \nabla.\left[\left(\mu + \frac{\mu_t}{\sigma_k}\right)\nabla k\right] + P_k - \beta^* \rho \omega k \tag{4}$$

where k is turbulent kinetic energy, μ_t is turbulent viscosity, σ_k is model constant controlling diffusion, P_k is Production of

turbulent kinetic energy, β* is Model constant (β* = 0.09) and ω is Specific Dissipation Rate, described by:

$$\nabla \cdot (\rho u \omega) = \nabla \cdot [(\mu + \frac{\mu_t}{\sigma_\omega})\nabla \omega] + \alpha \frac{\omega}{k} P_k - \beta \rho \omega^2 + 2(1 - F_1) \frac{\rho}{\sigma_{\omega 2}} \frac{\nabla k \cdot \nabla \omega}{\omega} \quad (5)$$

where α, β, and σ are Model constants. Also, F_1 is blending function switching between k-ω and k-ε models. Here, μ_t is the turbulent viscosity, modeled as:

$$\mu_t = \frac{\rho k}{\omega} \cdot \frac{1}{max(\frac{1}{\alpha^*}, \frac{SF_2}{a_1 \omega})} \quad (6)$$

where S is strain rate magnitude, F_2 is Second blending function and a_1 is model constant (a_1 = 0.31).

Boundary conditions at the airfoil surface include the no-slip condition for velocity (u = v = 0). For turbulent kinetic energy and specific dissipation rate, the applied boundary conditions are as below:

$$k = 0 \quad (7)$$

$$\omega = (\frac{\nu}{u_t^2}) \cdot (\frac{1}{\beta^*}) \quad (8)$$

where u_τ is the friction velocity. To incorporate the effect of the plasma actuator, the force term fx and fy are modeled using the Shyy-modified body force formulation [17], which converts the applied electric potential into a localized momentum source. The User Defined Function (UDF) used in this study, is as same as UDF used by Ebrahimi and Hajipour [16]:

$$|\vec{E}| = E_0 - k_1 x - k_2 y \quad (9)$$

$$\vec{F} = \rho_c e_c \vartheta \Delta T \vec{E} \quad (10)$$

$$|\vec{E}| = \left(\frac{|\vec{E}| k_2}{\sqrt{k_1^2 + k_2^2}} . \frac{|\vec{E}| k_1}{\sqrt{k_1^2 + k_2^2}} . 0 \right) \quad (11)$$

where ρ_c is charge density of electrons, e_c is elementary charge, ϑ is frequency of applied voltage and ΔT is discharge time.

Electrode parameters are defined relative to the airfoil chord: electrode length l_e/c = 0.07, thickness t_e/c = 0.00025, with maximum voltage of 5.7 kV at the wall (y = 0). These values are selected to ensure a physically realistic force profile and maintain a non-zero actuation effect in the numerical model.

2.2 Configuration and Numerical Domain

The present study investigates the influence of plasma actuator location and freestream velocity on the aerodynamic performance of a NACA 6412 airfoil. The test cases are summarized in Table 1. Four actuator positions are defined relative to the airfoil chord length and maximum camber location (40% chord for NACA 6412). The Leading Edge Left (LEL) position at x/c = 3% is located just downstream of the leading edge on the upper surface. The Leading Edge Right (LER) position at x/c = 10% lies further downstream but still upstream of the maximum camber. The Trailing Edge Left (TEL) position coincides with the maximum camber at x/c = 40%, while the Trailing Edge Right (TER) position at x/c = 65% is situated between the maximum camber and the trailing edge.

Table 1. Test cases for actuator placement and freestream velocity.

Case	Actuator Location (x/c)×100	Freestream Velocity
Baseline Airfoil	-	1 and 10 m/s
Leading Edge Left (LEL)	3%	1 and 10 m/s
Leading Edge Right (LER)	10%	1 and 10 m/s
TrailingEdge Left (TEL)	40%	1 and 10 m/s
TrailingEdge Right (TER)	65%	1 and 10 m/s

The plasma actuators are arranged in a spanwise configuration, with electrodes aligned perpendicular to the freestream direction. This configuration produces a streamwise-directed wall jet, directly energizing the boundary layer and enhancing near-wall momentum. Such an arrangement is commonly employed for delaying flow separation and controlling stall [18]. Figure 2 illustrates the actuator locations for all test cases.

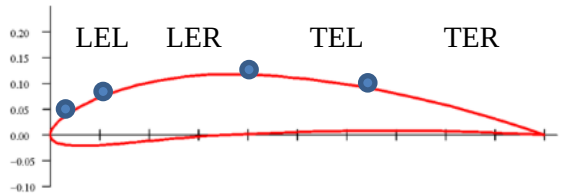

Fig. 2. Locations of plasma actuators on the NACA 6412 airfoil (spanwise configuration).

The computational domain employs a C-type topology, refined around the airfoil using the Body-of-Influence approach. A structured quadrilateral mesh with over 620,000 elements is generated to ensure numerical stability and computational efficiency. In addition to the Inflation layers, the Mesh Refinement is applied to wall surface of airfoil to fully resolve the viscous sublayer, enabling accurate prediction of separation and reattachment. The mesh is shown in Figure 3.

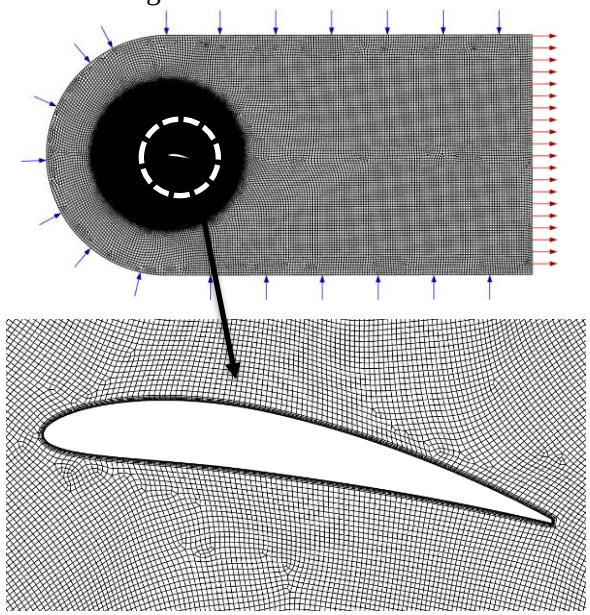

Fig. 3. C-type computational domain and mesh refinement around the NACA 6412 airfoil.

The Shear Stress Transport (SST) k–ω turbulence model is employed due to its high accuracy in simulating flows with adverse pressure gradients and separation. Near-wall resolution is verified by evaluating the non-dimensional wall distance Y^+. As shown in Figure 4, the maximum Y^+ is 1.6, with an average of 0.2, which satisfies the requirements for fully resolving the viscous sublayer in the SST k–ω model. All simulations are performed using a steady-state, pressure-based solver with a coupled algorithm for momentum and continuity equations.

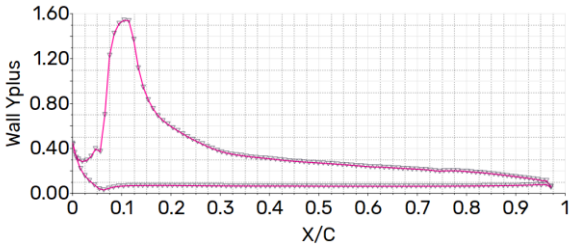

Fig. 4. Distribution of Y^+ on NACA 6412 airfoil surface.

3 RESULTS and DISCUSSION

3.1 Baseline Cases

As described in Section 2, two free-stream velocities (U_∞ = 1 and 10 m/s) and four chordwise actuator locations were examined. We begin with the baseline airfoil without flow control. Figures 5 and 6 show velocity streamlines colored by U/U_∞. In both cases a separated wake forms downstream, and a marked velocity deficit is visible over the suction side near the trailing edge, which explains the elevated drag.

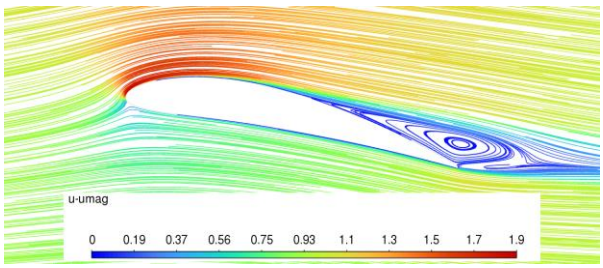

Fig. 5. Baseline, U_∞=1 m/s: velocity streamlines colored by U/U_∞.

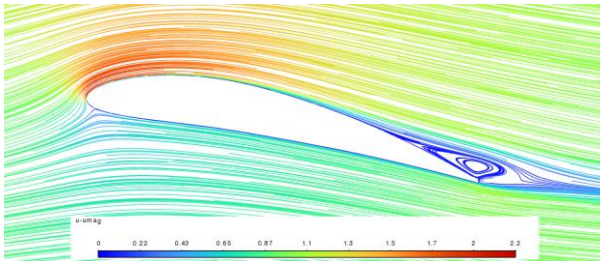

Fig. 6. Baseline, U_∞=10 m/s: velocity streamlines colored by U/U_∞.

The wall-normal gradient of streamwise velocity at the wall, $\partial u/\partial y$, is a compact indicator of attachment. Figures 7 and 8 reveal that at U_∞ = 1 m/s separation begins around x/c ≈ 0.60, whereas at U_∞ = 10 m/s it shifts aft to x/c ≈ 0.70. This later separation at the higher speed is consistent with a fuller near-wall velocity profile and greater local momentum, even though the adverse pressure gradient is stronger at α = 12°.

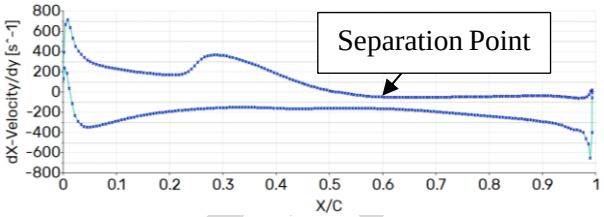

Fig. 7. Case Baseline Airfoil 1 m/s, $\partial u/\partial y$ velocity derivative

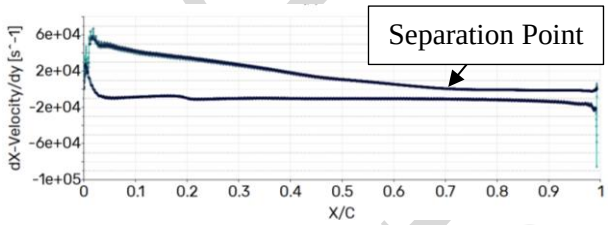

Fig. 8. Case Baseline Airfoil 10 m/s, $\partial u/\partial y$ velocity derivative

Surface-pressure evidence supports this interpretation. Figure 9 compares Cp distributions for the two baseline conditions. The 10 m/s case exhibits a deeper suction peak and steeper adverse gradient than the 1 m/s case, yet the added momentum delays separation relative to the lower-speed condition.

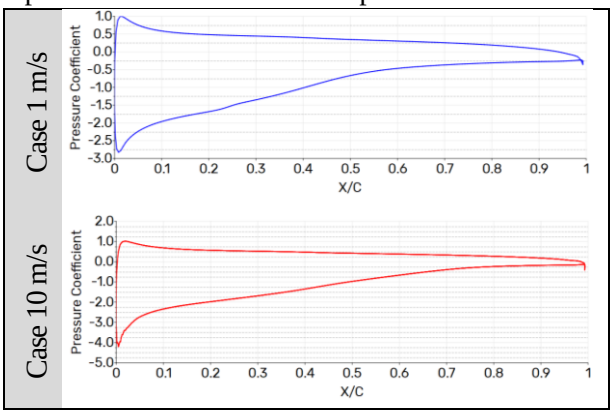

Fig. 9. Baseline Cp distributions at U_∞ = 1 and 10 m/s

3.2 Plasma actuator enabled

For U_∞ = 1 m/s, both LER and LEL remove the trailing-edge wake and produce attached flow along the suction side (Figures 10 and 11). The induced wall jet is much faster than the free-stream, so it dominates the near-wall region and overwhelms the incipient separation. LEL imparts a slightly stronger wall-jet signature than LER at this speed, which is consistent with its closer proximity to the leading edge and a thinner boundary layer at x/c ≈ 0.03.

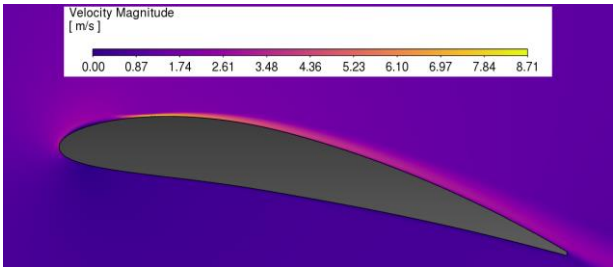

Fig. 10. LER, U_∞ = 1 m/s: velocity contour.

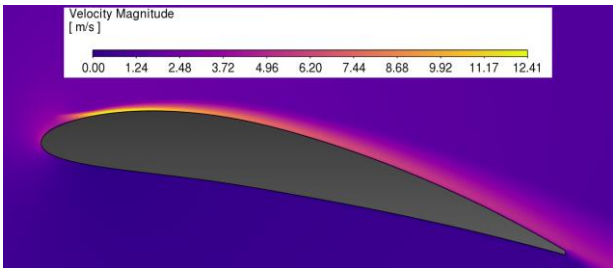

Fig. 11. LEL, U_∞ = 1 m/s: velocity contour.

At U_∞ = 10 m/s, placement becomes critical. As shown in Figures 12 and 13, LER does not fully remove separation; a residual separated zone persists near the trailing edge. In contrast, LEL prevents separation and yields a clean recovery. The mechanism is straightforward: near x/c ≈ 0.03 the boundary layer is thin and the actuator can energize essentially its full thickness while also coupling some momentum into the outer flow. By x/c ≈ 0.10 the layer is thicker and the same forcing acts on a more developed profile, which reduces authority.

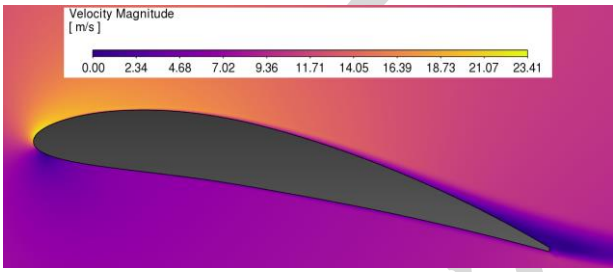

Fig. 12. LER, U_∞ = 10 m/s: velocity contour.

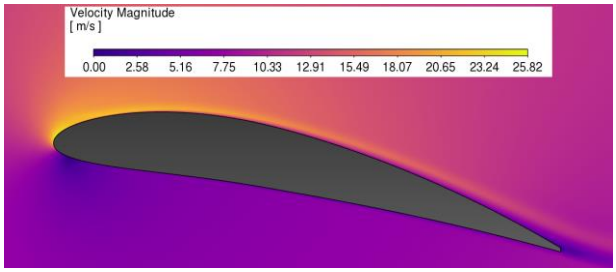

Fig. 13. LEL, U_∞ = 10 m/s: velocity contour.

The pressure distributions in Figures 14 and 15 corroborate this behavior. For U_∞ = 10 m/s, LEL shows a stronger suction peak (about −6.5 versus −5 for LER) and no indication of trailing-edge separation. The LER curve shows recovery that flattens near x/c ≈ 0.85, consistent with residual separation.

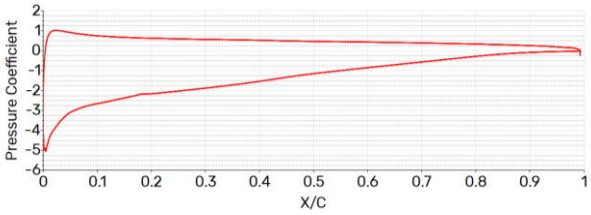

Fig. 14. LER, U_∞ = 10 m/s: surface Cp.

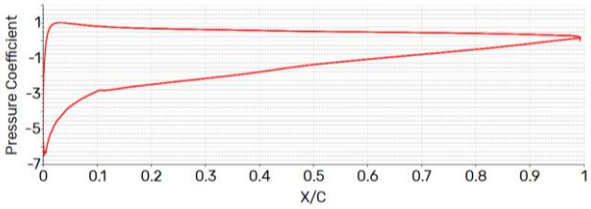

Fig. 15. LEL, U_∞ = 10 m/s: surface Cp.

Figures 16–19 examine the two downstream placements at 1 m/s. Both TER and TEL suppress large-scale separation over the airfoil, but each produces a laminar separation bubble near the leading edge. From the Cp distribution for TEL (Figure 17), the bubble extends approximately 0≤x/c≤0.20. For TER, the bubble is larger, extending to about x/c ≈ 0.4 (Figures 18–19).

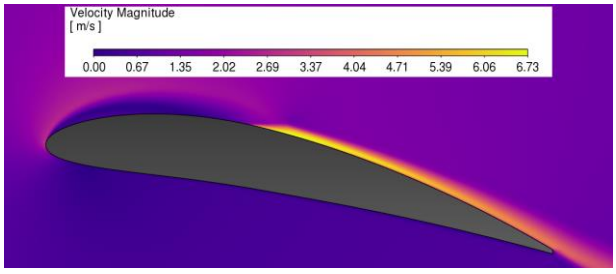

Fig. 16. TEL, U_∞ = 1 m/s: velocity contour.

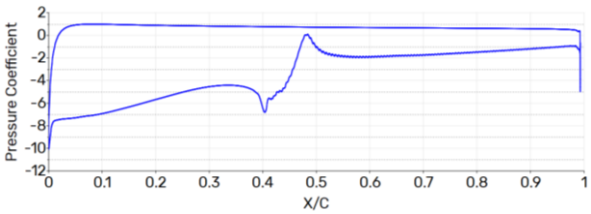

Fig. 17. TEL, U_∞ = 1 m/s: surface Cp.

This behavior is characteristic of very strong wall-jet actuation relative to the free-stream. When the induced jet speed greatly exceeds U_∞ and the actuator is located aft of the maximum thickness, streamlines upstream are bent toward the wall at the forcing location. The resulting adverse near-wall curvature promotes a local recirculation region that appears as a laminar separation bubble. The bubble increases pressure drag even if lift rises.

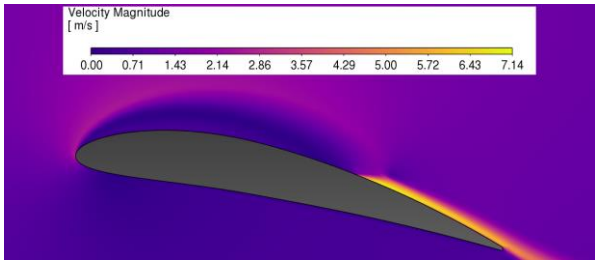

Fig. 18. TER, U_∞ = 1 m/s: velocity contour.

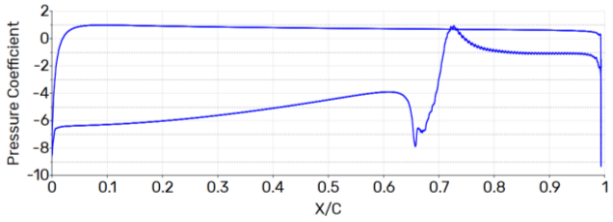

Fig. 19. TER, U_∞ = *1 m*/s: surface Cp.

At the higher free-stream speed, TER outperforms TEL (Figures 20–23). TER sits just upstream of the baseline separation point and injects momentum where it is most needed, so separation is prevented and pressure recovery is smooth. TEL is less effective because it lies farther from the incipient separation location; its forcing does not target the critical region as precisely. Comparing the Cp curves for TEL and TER at 10 m/s shows that TER attains a deeper suction peak and a more monotonic recovery without trailing-edge signatures of separation.

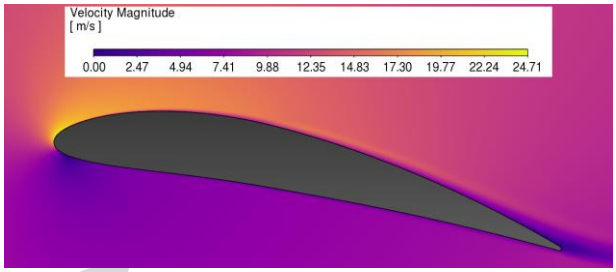

Fig. 20. TEL, U_∞ = 10 m/s: velocity contour.

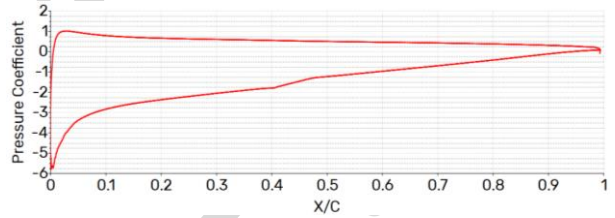

Fig. 21. TEL U_∞ = 10 m/s: surface Cp.

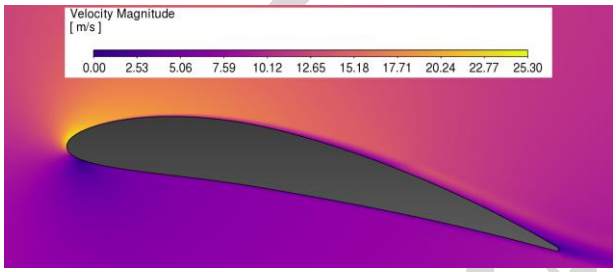

Fig. 22. TER, U_∞ = 10 m/s: velocity contour.

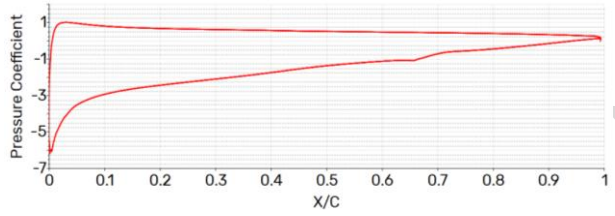

Fig. 23. TER U_∞ = 10 m/s: surface Cp.

Generally, for wall-jet-based separation control and pressure recovery on an airfoil, it is desirable that the actuator promotes a gradual pressure recovery without sharp fluctuations in the surface pressure distribution. This requires selecting an actuation strength commensurate with the local flow momentum; in practice, a jet velocity of the same order as the free-stream is effective, as in the U_∞=10 m/s cases examined here. When actuators of comparable strength are compared across chordwise locations, the 10 m/s results show that LEL and TER provide the most robust separation control and the smoothest recovery. By contrast, overly strong forcing aft of the maximum thickness can bend upstream streamlines toward the wall and generate a laminar separation bubble, which increases drag despite possible lift gains.

Figures 24 and 25 summarize the changes in lift and drag, normalized by their baseline values. At 1 m/s, using an actuator strength that is far larger than the local flow momentum can raise C_d even when C_l increases, which does not yield a beneficial operating point. At 10 m/s the picture is more favorable: LEL and TER produce the largest lift gains with concurrent drag reduction, because they either energize the thin boundary layer early (LEL) or add momentum right before natural separation (TER). LER is the least effective across these comparisons, particularly at 10 m/s, because it neither pre-conditions the boundary layer sufficiently early nor targets separation onset.

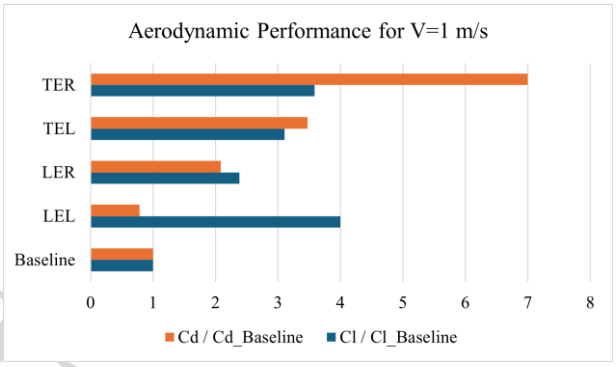

Fig. 24. $C_l/C_{l\ Baseline}$ and $C_d/C_{d\ Baseline}$ at U_∞ = 1 m/s for different cases.

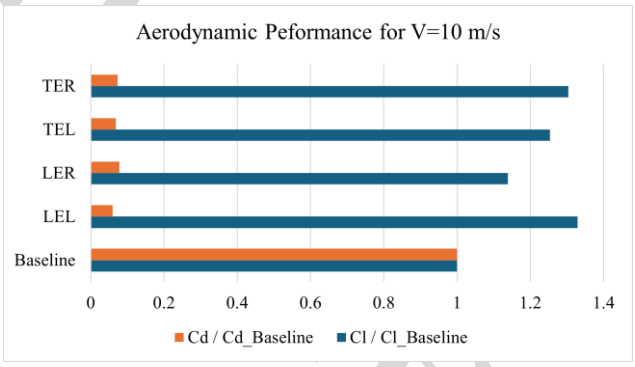

Fig. 25. $C_l/C_{l\ Baseline}$ and $C_d/C_{d\ Baseline}$ at U_∞ = 10 m/s for different cases.

Two practical lessons follow. First, match actuation strength to the local momentum level so that pressure recovery remains gradual; excessive

forcing aft of the maximum thickness can trigger laminar separation bubbles and increase drag. Second, for single-actuator layouts on a cambered airfoil at moderate incidence, a leading-edge placement near x/c ≈ 0.03 or a downstream placement just upstream of the baseline separation point (here x/c ≈ 0.65) provides the most robust control.

4 CONCLUSION

This study examined how the chordwise placement of a single DBD plasma actuator affects separation control on a cambered NACA 6412 airfoil at $\alpha = 12°$ for $U_\infty = 1$ and 10 m/s using steady RANS (SST k–ω) simulations with a Shyy-type body-force model. The results show that actuator position strongly governs authority by setting where and how momentum is added to the boundary layer.

• A leading-edge placement at x/c ≈ 0.03 (LEL) consistently provided the best overall outcome, earlier boundary-layer energization, suppression of separation, stronger suction peak, and smoother pressure recovery.

• A downstream placement near x/c ≈ 0.65 (TER) was the second-best option, because it targets the vicinity of the natural separation onset.

• For actuator placements aft of the maximum thickness (x/c ≳ 0.40), and at low U_∞ a very strong actuation that generates a plasma jet much faster than the free-stream can induce a laminar separation bubble and increase drag despite lift gains.

Design guidance therefore favors (i) a leading-edge actuator for robust, early energization or (ii) a downstream actuator positioned just upstream of the baseline separation point. Matching actuation strength to local momentum is essential to achieve gradual pressure recovery and minimize drag penalties. Future work should explore multiple actuators, unsteady/multi-frequency excitation, and three-dimensional effects, together with experimental validation, to generalize these placement strategies.

CONFLICT OF INTEREST

The authors declare that they have no conflict of interest.

5 REFERENCES

[1] A. Tayebi and F. Torabi, “Flow control techniques to improve the aerodynamic performance of Darrieus vertical axis wind turbines: A critical review,” *J. Wind Eng. Ind. Aerodyn.*, vol. 252, p. 105820, 2024.

[2] J. Poggie, T. McLaughlin, and S. Leonov, “Plasma aerodynamics: current status and future directions,” *Aerosp. Lab*, no. 10, 2015.

[3] K.-S. Choi *et al.*, “Plasma virtual actuators for flow control,” *J. Flow Control. Meas. Vis.*, vol. 3, no. 01, p. 22, 2014.

[4] T. C. Corke, C. L. Enloe, and S. P. Wilkinson, “Dielectric barrier discharge plasma actuators for flow control,” *Annu. Rev. Fluid Mech.*, vol. 42, no. 1, pp. 505–529, 2010.

[5] G. Neretti, “Active flow control by using plasma actuators,” *Recent Prog. Some Aircr. Technol.*, vol. 1, p. 13, 2016.

[6] Y. Bouremel, J. M. Li, Z. Zhao, and M. Debiasi, “Effects of AC Dielectric Barrier Discharge plasma actuator location on flow separation and airfoil performance,” *Procedia Eng.*, vol. 67, pp. 270–278, 2013.

[7] K. V Karthikeyan and R. Harish, “Enhanced aerodynamic performance of NACA4412 airfoil through integrated plasma actuator and Gurney flap flow control,” *Results Eng.*, vol. 25, p. 103977, 2025.

[8] T. Ogawa, K. Asada, M. Sato, T. Tatsukawa, and K. Fujii, “Computational study of the plasma actuator flow control for an airfoil at pre-stall angles of attack,” *Appl. Sci.*, vol. 12, no. 18, p. 9073, 2022.

[9] X. N. Wang, W. B. Wang, Y. Huang, Z. B. Huang, and Z. H. Sheng, “Airfoil flow control using DBD plasma actuators,” in *Fluid-Structure-Sound Interactions and Control: Proceedings of the 2nd Symposium on Fluid-Structure-Sound Interactions and Control*, Springer, 2013, pp. 141–147.

[10] R. Khoshkhoo and A. Jahangirian, “Numerical simulation of flow separation control using multiple DBD plasma actuators,” *J. Appl. Fluid Mech.*, vol. 9, no. 4, pp. 1865–1875, 2016.

[11] C. Kelley *et al.*, “High Mach number leading-edge flow separation control using AC DBD plasma actuators,” in *50th AIAA Aerospace Sciences Meeting Including the New Horizons Forum and Aerospace Exposition*, 2012, p. 906.

[12] J. Little, M. Nishihara, I. Adamovich, and M. Samimy, “High-lift airfoil trailing edge

separation control using a single dielectric barrier discharge plasma actuator," *Exp. Fluids*, vol. 48, pp. 521–537, 2010.

[13] G. Yu, D. Li, and Z. Zhang, "Numerical simulation for the differences between FTN/WPN engine models aerodynamic influence on BWB300 airframe," *Eng. Appl. Comput. Fluid Mech.*, vol. 14, no. 1, pp. 566–579, 2020.

[14] J. Basic, "Turbulent history of fluid mechanics (brief essay)," *Retrieved Novemb.*, vol. 25, p. 2018, 2016.

[15] S. Khasare, F. Bagherighajari, F. Dolati, J. Mahmoudimehr, J. Páscoa, and M. Abdollahzadehsangroudi, "The effect of the dielectric barrier discharge plasma actuator in the control of non-reactive flow in a non-premixed bluff body burner," *Phys. Fluids*, vol. 35, no. 7, 2023.

[16] A. Ebrahimi, and M. Hajipour, "Flow separation control over an airfoil using dual excitation of DBD plasma actuators", *Aerospace Science and Technology, 79*, pp.658-668, 2018.

[17] W. Shyy, B. Jayaraman, and A. Andersson, "Modeling of glow discharge-induced fluid dynamics," *J. Appl. Phys.*, vol. 92, no. 11, pp. 6434–6443, 2002.

[18] A. Ebrahimi, M. Hajipour, & K. Ghamkhar, "Experimental study of stall control over an airfoil with dual excitation of separated shear layers," *Aerospace Science and Technology, 82*, 402-411, 2018.